Dalton Transactions

RSC Publishing

PAPER

View Article Online
View Journal | View Issue

Cite this: *Dalton Trans.*, 2013, **42**, 16920

Cyanamide route to calcium–manganese oxide foams for water oxidation†

Elham Baktash,[a] Ivelina Zaharieva,*[b] Marc Schröder,[c] Caren Goebel,[a] Holger Dau*[b] and Arne Thomas*[a]

In nature, photosynthetic water oxidation is efficiently catalysed at a protein-bound μ-oxido Mn_4Ca cluster. This cluster consists of earth abundant, non-toxic elements and serves as a paragon for development of synthetic catalysts. In this study we developed porous calcium–manganese oxides with a unique foam-like nanostructure prepared *via* a facile and robust synthetic route using cyanamide as a porogen. A series of such oxide foams annealed at different temperatures was characterized by TEM, SEM, XRD, N_2 physisorption, and X-ray absorption spectroscopy (XAS) in order to correlate crystallinity, atomic structure, surface area and oxidation state of the materials with catalytic activity. Some of the resulting Ca–Mn oxides show high activity as catalysts for water oxidation in the presence of cerium(IV) ammonium nitrate as a non-oxo transfer oxidant. An amorphous calcium–manganese-oxide foam with 130 $m^2\ g^{-1}$ surface area and Mn oxidation state of +3.6 was identified to be most active; its activity is superior to previously reported Ca–Mn oxides. At the atomic level, this material shares structural motifs with the biological paragon as revealed by dual-edge XAS at the Mn and Ca K-edge. Rather than nanostructure and surface area, the atomic structure of the Ca–Mn oxide and the extent of structural order appear to be crucial determinants of catalytic activity. Fully disordered low-valent Mn materials as well as high-valent but crystalline Mn–Ca oxides are unreactive. Highly disordered variants of layered manganese oxide with Ca and water molecules interfacing layer fragments are most reactive.

Received 25th June 2013,
Accepted 28th August 2013

DOI: 10.1039/c3dt51693h

www.rsc.org/dalton

Introduction

Dioxygen formation by catalytic water oxidation is an essential half reaction for important processes such as water splitting or artificial photosynthesis.[1] Beside noble metals (RuO_2,[2] IrO_2,[3] *etc.*), transition metal oxides, such as cobalt,[4] manganese[5–7] and nickel oxides,[8] have been shown to be active and robust catalysts for this reaction. For example, MnO_2 [9] and Mn_2O_3 [5] catalyse water oxidation in the presence of different oxidizing agents. Following these pioneering studies different manganese oxides have been prepared which show promising activity towards water oxidation in the presence of non-oxo transfer oxidants, for example λ-MnO_2,[10] α-MnO_2 nanowires and nanotubes, β-MnO_2 nanowires,[11] nano-sized α-Mn_2O_3 [12] and amorphous manganese oxides.[13]

Often metal oxides with a high level of amorphicity at both the nanostructural and atomic level showed high activity but the insight into structure–reactivity relationships has remained insufficient. On the other hand, well-ordered (diffracting) manganese hydroxides and oxides showed catalytic activity in water oxidation, but only at comparatively low level.[14–17] Inspired by the biological catalysts bound to the proteins of photosystem II, the photosynthetic $Mn_4Ca(\mu\text{-}O)_n$ cluster,[18] calcium–manganese oxides have been also studied as water oxidation catalysts. Indeed, it has been recently shown that incorporation of calcium ions can improve the catalytic activity of synthetic Mn oxides pronouncedly, but only for the formation of amorphous Ca–Mn oxides.[19,20]

Increasing the surface area of heterogeneous catalysts, either by forming smaller particles or by creating pores, is a practical pathway to increase the catalytic efficiency of solid materials. For the generation of porous materials most often templating approaches are applied. For example, the inorganic phase can be formed in the presence of an organic porogen, which afterwards is removed leaving behind more or less defined pores in the inorganic matrix. We have recently presented a pathway to prepare highly porous silicas in a one-step

[a]*Technische Universität Berlin, Department of Chemistry, Hardenbergstr. 40, 10623 Berlin, Germany. E-mail: arne.thomas@tu-berlin.de; Fax: +49 30 314 29271; Tel: +49 30 314 25118*

[b]*Freie Universität Berlin, Department of Physics, Arnimallee 14, 14195 Berlin, Germany. E-mail: ivelina.zaharieva@fu-berlin.de, holger.dau@fu-berlin.de; Fax: +49 30 838 56299; Tel: +49 30 838 53581*

[c]*Technische Universität Berlin, Department of Chemistry, Straße des 17. Juni 124, 10623 Berlin, Germany*

†Electronic supplementary information (ESI) available. See DOI: 10.1039/c3dt51693h

approach by adding cyanamide to a silica precursor solution and subsequent gelation and heat treatment of this mixture. Heat treatment of cyanamide yield, over several polycondensation steps, a polymeric carbon nitride, which acted as a hard template to create the porosity in the silica.[21] Herein we used a comparable approach, namely mixing Ca–Mn oxide precursors with cyanamide and additional heat treatment. However, here the organic porogen decomposed already at lower temperatures leaving behind a porous, foam-like Ca–Mn oxide. Different cyanamide/metal ratios were applied and the resulting Ca–Mn oxide foams were calcined at different temperatures, to obtain a series of oxides, which were tested as catalysts for water oxidation. The structure of the formed materials was investigated by X-ray absorption spectroscopy at the Mn and Ca K-edge, powder XRD and (HR)TEM and the results suggest that in this case the surface area is not the decisive factor that determines the catalytic activity.

Experimental section

Synthesis of $CaMn_2O_x$-*A*-*B*

0.687 g of $Mn(NO_3)_2{\cdot}4H_2O$ and 0.32 g of $Ca(NO_3)_2{\cdot}4H_2O$ were dissolved in 2 ml distilled water. To this solution an aqueous solution of different amounts of cyanamide (0.8, 4.0 and 8.0 g, conc. 1.0 g ml^{-1}, "*A*" denotes the amount of cyanamide used) was added and the resulting mixture was stirred for 3 h under air (pH = 1). The final solution was poured into a Petri dish and heated at 100 °C for 30 h. The resulting brown-grey solid is scratched from the Petri dish and calcined under ambient conditions at different temperatures (T_{calc} = 300 °C, 400 °C, 550 °C, 700 °C, 1000 °C, "*B*" denotes the applied calcination temperature). A heating ramp with the rate of 3 °C min^{-1} was used until the final temperature was reached and then the samples were heated for 4 h at this temperature.

Two reference materials were also prepared, one without cyanamide (*A* = 0) and the other without calcium.

Characterization

X-ray diffraction (XRD) patterns were measured in the reflection mode on a Bruker D8 Advance X-ray diffractometer using $CuK\alpha_1$ irradiation (λ = 0.154 nm). IR spectra were measured on a Varian 1000 FTIR spectrometer using an ATR technique.

The microstructure (morphology, crystallinity, particle size, and chemical composition) of the samples was studied by electron microscopy at the Department of Electron Microscopy ZELMI, TU Berlin. Transmission electron microscopy (TEM) measurements were performed using a FEI Tecnai G2 20 S-TWIN transmission electron microscope equipped with a LaB_6-source at 200 kV acceleration voltages. For TEM-investigations a small amount of the sample powder was placed on a TEM-grid (carbon film on 300 mesh Cu-grid, Plano GmbH, Germany) and was sputtered with carbon. EDX-analysis was carried out using an EDAX r-TEM SUTW Detector (Si (Li)-detector). Images were recorded using a GATAN MS794 P CCD-camera.

For scanning electron microscopy (SEM) analysis, a small amount of the sample powder was placed on a conducting carbon pad (Plano GmbH, Germany) and sputtered with a thin carbon layer. The investigations were performed by means of a JXA-8530F microprobe (JEOL GmbH, Germany) equipped with a field emission source. Qualitative chemical analysis and beam scan mapping were carried out at 20 kV acceleration voltage by integrated energy dispersive X-ray spectroscopy using a SDD detector.

Specific surface area of samples was determined at liquid-nitrogen temperature (−196 °C) using an Autosorb-1 Instrument. The sample was degassed at 150 °C overnight before measurement. The Brunauer–Emmett–Teller (BET) surface area was calculated by multiple-point (five-point) measurements in the relative pressure range of 0.05–0.30.

Thermogravimetric analysis (TGA) measurements were carried out using a STA6000 from Perkin-Elmer under ambient conditions at a temperature range of 30–1000 °C with the heating rate of 10 °C min^{-1}. The amount of metal in the samples was determined by inductively coupled plasma atomic emission spectroscopy, using an ICP-OES 517 (Varian Inc., USA).

X-ray absorption spectra (XANES/EXAFS) were collected at the BESSY synchrotron radiation source operated by the Helmholtz-Zentrum Berlin. The measurements were acquired at the KMC-1 bending-magnet beamline at 20 K in a cryostat (Oxford-Danfysik) with a liquid-helium flow system. The oxide powder samples were diluted by thoroughly mixing with boron nitride (BN) powder (Sigma Aldrich) to a ratio of 1 : 10. The measurements at the manganese K-edge were performed in the transmission mode with an ionization chamber and the spectra at the Ca K-edge were detected in the fluorescence mode using a 13-element energy-resolving Ge detector (Canberra). Further details are given in ref. 22.

Oxygen evolution was measured using a Clark-type oxygen electrode system (Strathkelvin, 1302 oxygen electrode and 782 oxygen meter). An air saturated water solution and zero-oxygen (sodium sulfite in water) solution were used for the calibration of the electrode. In a typical run oxygen evolution was detected with the electrode under stirring in an anaerobic solution of oxides in the presence of 0.5 M $(NH_4)_2Ce(NO_3)_6$ (see ESI†). An Agilent 7890A gas chromatograph was used to determine the oxygen content in the headspace of the reactor. The GC was equipped with a carboxen-1000 column and a thermal conductivity detector (TCD). The carrier gas was argon (30 mL min^{-1}). Calibration was done with an oxygen gas mixture of defined concentrations (1 and 10 vol%).[23]

Results and discussion

For the preparation of porous calcium manganese oxides, aqueous solutions of calcium and manganese(II) nitrates were mixed with cyanamide. After the removal of water (by evaporation at 100 °C), the resulting solid mixtures were heated at different temperatures (Scheme 1). Two series of calcium manganese oxides have been prepared using either different

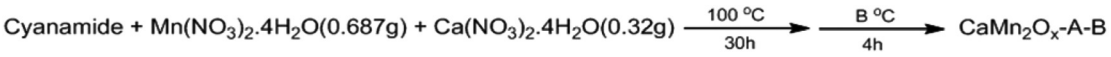

Scheme 1 Synthetic route of $CaMn_2O_x$-*A*-*B* with different amounts of porogen and various calcination temperatures (*A* = 0.8, 4 and 8 g, *B* = 300, 400, 550, 700, 1000 °C).

amounts of cyanamide or different calcination temperatures. Depending on the amount of used cyanamide and calcination temperature, samples are denoted $CaMn_2O_x$-*A*-*B* (*A* is the amount of cyanamide in grams and *B* is the calcination temperature in °C).

Similar to previous works of Kurz[19] and Shilov[9] we used simple Mn^{2+} and Ca^{2+} salts as precursors. However in our synthetic route we did not add an oxidant (MnO_4^-). Instead oxidation of Mn is induced by heating the Mn–Ca mixture in the presence of oxygen. When no cyanamide is added (*e.g.* $CaMn_2O_x$-0-550), a non-porous mixture of crystalline phases is formed, which just showed very low catalytic activity for water oxidation. However, the addition of cyanamide yield materials with an increased surface area and strongly affects the atomic structure of the formed oxides, which eventually results in the formation of highly active catalysts (see below).

It has been described that on thermal treatment, cyanamide transforms *via* several condensation steps into dicyandiamide, melamine, melem and finally into melon, a polymeric carbon nitride.[24,25] Such polymeric carbon nitrides are just formed at temperatures as high as 550 °C and have recently gained increasing interest for their applications as photocatalysts.[24] Decomposition of such carbon nitrides finally occurs at around 650 °C. However in the present system no formation of a polymeric carbon nitride was observed at temperatures above 300 °C. Indeed TGA measurements (Fig. S1†) and elemental analysis showed that only in the sample prepared at 300 °C ($CaMn_2O_x$-0.8-300) a considerable amount of organic moieties can be found, while already at 400 °C ($CaMn_2O_x$-0.8-400) only minor amounts of carbon and nitrogen residues are detectable (N%: 0.8, C%: 1.9) suggesting that the formed CaMn oxide accelerates decomposition of the carbon nitride precursors drastically. TGA measurement of the oxides heated to lower temperatures (300 °C/400 °C) also show considerable weight losses in the temperature range of 30–400 °C, which is explained by the loss of water weakly bound to the oxide layers. Further weight loss in the range of 400 °C to 1000 °C can be explained by phase transition with oxygen release *e.g.* by reduction of manganese from Mn^{4+} to Mn^{3+} and finally Mn^{2+}.[26]

In the infrared (IR) spectra (Fig. S2†), broad bands around 3300 cm^{-1} and 1640 cm^{-1} are assignable to O–H stretching and H–O–H bending mode vibrations of water. They are especially pronounced in $CaMn_2O_x$-0.8-400, confirming the presence of sizeable amounts of water. The vibrational modes of the MnO_6 units expand over the 700–400 cm^{-1} region, as expected for Mn oxides.[27] ICP-OES was carried out to determine the calcium and manganese content of the oxides and showed that the Ca : Mn ratio in calcium manganese oxides remained unchanged during the preparation process (Ca : Mn ~ 1 : 2) (Table S1†).

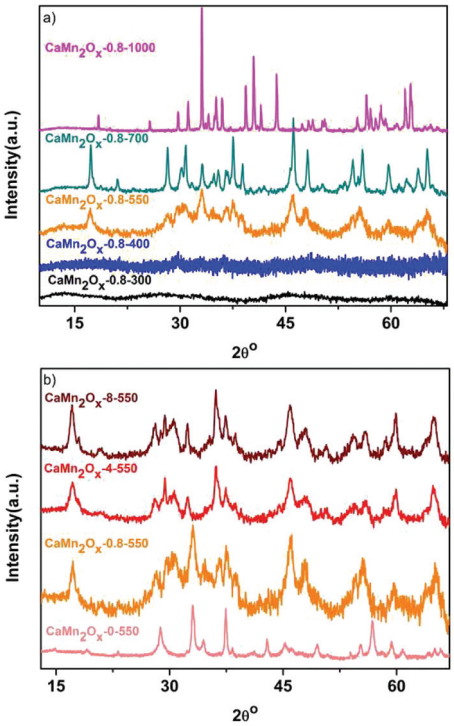

Fig. 1 XRD patterns of (a) $CaMn_2O_x$-0.8-*B* calcined at different temperatures and (b) $CaMn_2O_x$-*A*-550 prepared with different amounts of cyanamide porogen.

X-ray powder diffraction (XRD) was used to identify the formed oxide phases. Fig. 1a shows the XRD patterns of samples produced with a constant amount of cyanamide but at different calcination temperatures ($CaMn_2O_x$-0.8-*B*). The oxide heated to 300 °C is completely XRD amorphous. By heating the sample to 400 °C, a broad peak of low intensity at 2θ = 29.4° may be observable, which cannot be easily assigned. Partial crystallisation (lowered amorphicity) of the samples is observed for oxides heated to 550 °C. At 700 °C, the XRD peaks become more intense and can be finally assigned to a layered $Ca_2Mn_3O_8$ structure (Fig. S3†).[28,29] Further heating to 1000 °C yielded a complete phase change from $Ca_2Mn_3O_8$ to $CaMn_2O_4$ (Fig. S4†).

XRD patterns of the oxides heated to 550 °C and prepared with different amounts of cyanamide are shown in Fig. 1b ($CaMn_2O_x$-*A*-550). All patterns point toward the presence of $Ca_2Mn_3O_8$, however the broad peaks again point toward a high level of amorphicity.

The broad XRD peaks are explainable either by very small crystallites (see 'crystal size' in Tables 1 and 2) or by structural disorder (amorphicity) at the atomic level resulting, *e.g.*, from a high number of defect sites or lack of a well-defined unit cell. The XRD pattern generally reflects the pair distribution

Table 1 Characterization of oxides prepared at different calcination temperatures

Catalyst	S_{BET}[a]	Oxygen evolution rate[b]	Crystal size[c]	Oxidation state	Parent phase
$CaMn_2O_x$-0.8-300	0.2	0.011	Amorphous	2.1[f]	Mn^{2+} and Ca^{2+} in the amorphous organic matrix
$CaMn_2O_x$-0.8-400	130	3.0/0.42[d]	Amorphous, <5[e]	3.6[f]	Layer-type $CaMn_2^{III/IV}$ oxide, fully amorphous
$CaMn_2O_x$-0.8-550	62	0.62	5–18	3.7[f]	Similar $Ca_2Mn_3O_8$
$CaMn_2O_x$-0.8-700	19	0.082	17–53	3.8[f]	$Ca_2Mn_3O_8$
$CaMn_2O_x$-0.8-1000	3.3	0.018	40–93	3[g]	$CaMn_2O_4$ (marokite)
Mn_2O_3-0.8-550	36	0.10	15–38	3[g]	Mn_2O_3

[a] Surface area of oxides ($m^2\ g^{-1}$). [b] Oxygen evolution rate ($mmol_{O2}\ mol_{Mn}^{-1}\ s^{-1}$) in the presence of $[Ce^{4+}]$ = 0.5 M. [c] Crystal size (nm) calculated based on the Scherrer equation of XRD peaks. [d] Oxygen evolution rate ($mmol_{O2}\ mol_{Mn}^{-1}\ s^{-1}$) in the presence of $[Ce^{4+}]$ = 0.5 M resulted from long-term measurement by gas chromatography (Fig. S15 and Table S4). [e] Crystal or particle size as estimated from (HR)TEM image. [f] Oxidation state based on XANES data. [g] Oxidation state as deduced from XRD results (Fig. S3–5).

Table 2 Characterization of oxides prepared with different amounts of porogen

Catalyst	S_{BET}[a]	Oxygen evolution rate[b]	Crystal size[c]	Oxidation state	Resolved parent phase(s)
$CaMn_2O_x$-8-550	46	0.14	11–39	—	$Ca_2Mn_3O_8$
$CaMn_2O_x$-4-550	51	0.22	7–27	—	$Ca_2Mn_3O_8$
$CaMn_2O_x$-0.8-550	62	0.62	5–18	3.7[d]	$Ca_2Mn_3O_8$
$CaMn_2O_x$-0-550	3.9	0.029	16–66	3.9[e]	Mixture of oxide phases[f]

[a] Surface area of oxides ($m^2\ g^{-1}$). [b] Oxygen evolution rate ($mmol_{O2}\ mol_{Mn}^{-1}\ s^{-1}$) in the presence of $[Ce^{4+}]$ = 0.5 M. [c] Crystal size (nm) calculated based on the Scherrer equation of XRD peaks. [d] Oxidation state based on XANES data. [e] Oxidation state as deduced from XRD results (Fig. S3–5). [f] XRD reflections were assigned to MnO_2, Mn_2O_3, Ca_2MnO_4, and CaO; alternative assignments are not excluded.

function (PDF) of the atoms in the diffracting material; for ideal XRD data, the PDF can be obtained directly from the XRD pattern by appropriate Fourier transformation. For non-crystalline samples of limited long-range order, broad reflections may be observable which are assignable to the 'parent structure' of a crystalline material. Accordingly we suggest that the temperature increase from 400 °C *via* 550 °C to 700 °C (Fig. 1a) results in increasing similarity of the material to the same parent structure, namely $Ca_2Mn_3O_8$. This suggestion is supported by the EXAFS data presented further below. (Here and in the following, we use the term 'parent structure' to denote a crystalline material which contains a set of structural motifs also found in the amorphous materials. In the amorphous material however, mixed oxidation states, the presence of water molecules, and other factors result in a low degree of order such that the structural motifs of the parent structure become less prominent.)

As seen in Fig. 1b, more intense but still broadened peaks for the layered $CaMn_2O_x$ are observed with an increasing amount of cyanamide. Alternatively, when no cyanamide was added ($CaMn_2O_x$-0-550) the formation of a phase resembling $Ca_2Mn_3O_8$ is not observed anymore. Instead reflections assignable to different Mn and Ca oxide phases or parent structures are observed (Table 2, Fig. S5†). XRD analysis thus shows that the addition of cyanamide to the precursor mixture not only introduces porosity (see below) but is also responsible for a phase change of the Ca–Mn oxides during heat treatment.

Calcium manganese oxides have been prepared without the addition of cyanamide.[19] These oxides showed a long range metal–metal interaction at 400 °C and even at 60 °C which indicates the formation of pre-ordered structures already at low temperature.[30] In the herein described protocol, cyanamide condensation forms an organic framework below 400 °C and metal ions are at this stage most likely coordinated to the building blocks of the framework (Tri-s-triazines, melamine, *etc.*). This results in their spatial separation and therefore inhibition of the formation of any specific oxide phase. In fact, no long-range metal–metal interaction can be found in the composites until the calcination temperature approaches 550 °C (see below). By heating the sample to 400 °C the organic network decomposes and a calcium manganese oxide with highly disordered nature is formed, proven by XRD and XAS. Thus the formation of different phases of CaMn oxide with and without cyanamide might be explained by the very different temperatures at which the first formation of long-range order and eventually crystallization occurs.

Transmission electron microscopy (TEM) was used to reveal the structure of the materials (Fig. 2 and Fig. S6–8†). $CaMn_2O_x$-0.8-300 shows no distinct features, but a rather intimate mixture between Ca–Mn oxide and carbon nitride precursors at this temperature. As mentioned before, between 300 °C and 400 °C the organic phase disappears forming gaseous decomposition products and nearly pure Ca–Mn oxide remains. Indeed $CaMn_2O_x$-0.8-400 shows a foam-like structure as it is typically observed in polymers when gaseous products are formed during polymerization. The foam structure can be also observed by SEM measurements (Fig. 2f). When heated to 550 °C, the porous structure becomes denser, with an average decrease in the pore size that may be due to the reduced amorphicity and water loss of the material resulting in structural contraction. At 700 °C the foam or porous structure completely

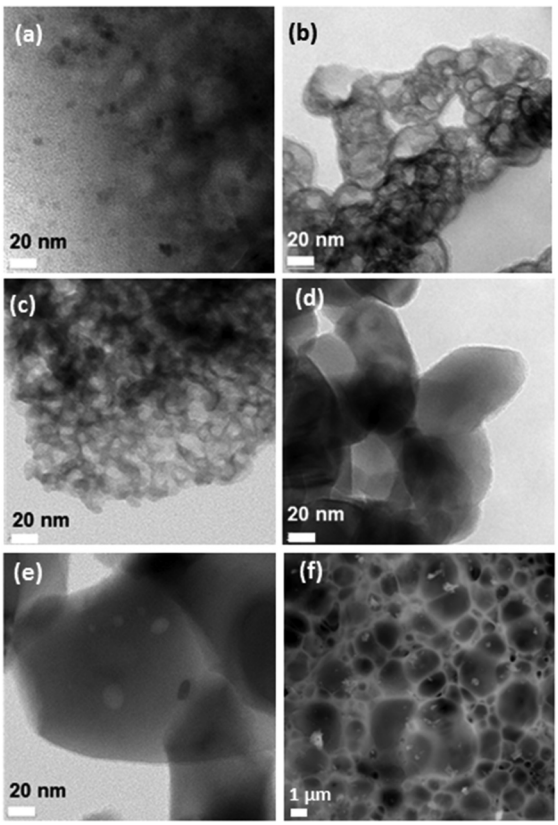

Fig. 2 (a–e) TEM images of calcium manganese oxide samples which were calcined at (a) 300 °C, (b) 400 °C, (c) 550 °C, (d) 700 °C, (e) 1000 °C, (f) SEM images of $CaMn_2O_x$-0.8-400.

disappears and instead larger particles are observed. EDS-mapping images (Fig. S9–S11†) prove a homogenous distribution of calcium, manganese and oxygen within all the samples calcinated at temperatures above 300 °C, rendering a phase separation, *e.g.*, between one calcium oxide and one or more manganese oxides unlikely. While in the XRD no reflections are observed for $CaMn_2O_x$-0.8-400, (HR)TEM images analyzed by fast Fourier-transformation reveal a diffuse diffraction ring and weak diffraction reflexes corresponding to *d*-values of the $Ca_2Mn_3O_8$ phase (Fig. S7†). The *d*-value of 2.9 Å is in agreement with the EXAFS results revealing a prominent Mn–Mn distance of 2.87 Å. (HR)TEM images of the samples $CaMn_2O_x$-0.8-550 and $CaMn_2O_x$-0.8-700 confirm the XRD results; they suggest the presence of a layered $Ca_2Mn_3O_8$ (parent) structure (Fig. S8†). This structure can be described as vacancy-containing sheets of edge-sharing MnO_6 octahedra which are interconnected by Ca^{2+} ions[28,29] (Fig. S12†).

Nitrogen sorption experiments showed that the herein presented preparation method resulted in oxides with increased surface areas (Tables 1 and 2). While from the pure Ca and Mn salts, Ca–Mn oxides (*e.g.* $CaMn_2O_x$-0-550) with lower outer surface areas (~4 m^2 g^{-1}) are observed, the addition of cyanamide yields surface areas up to 130 m^2 g^{-1} for $CaMn_2O_x$-0.8-400 and 62 m^2 g^{-1} for $CaMn_2O_x$-0.8-550. The chosen amount of 0.8 g cyanamide seems to be optimal for creating the porous structure as a further increase does not yield higher surface areas. A higher amount of template of course yields thinner pore walls in the replica. Thus, when a certain cyanamide/metal ratio is reached, structural collapse and a decrease in the overall surface area can be observed. As confirmed by electron microscopy measurements, the porosity of the samples collapsed when prepared with higher amounts of cyanamide (Fig. S6†) or at higher temperatures, *i.e.* at 700 °C and 1000 °C (Fig. 2) and consequently lower surface areas and porosities are observed.

We note that the achieved surface area of 130 m^2 g^{-1} for $CaMn_2O_x$-0.8-400 is still lower than the surface area of previously reported MnCa oxides[19] with surface areas of 205 m^2 g^{-1} or 303 m^2 g^{-1}. In spite of the lower surface areas, the MnCa oxides described herein excel by clearly higher oxygen evolution activity (Table S2†), as discussed in the following.

Oxygen evolution

Water-oxidation experiments were carried out in the presence of a non-oxygen transfer oxidizing agent, cerium ammonium nitrate, to investigate the catalytic activity of the oxides (Fig. 3, S13† and Tables 1, 2 and S2, 3†). Ce^{4+} is a single electron oxidant with a high oxidation potential (Ce^{4+}/Ce^{3+}, E_0 ~ +1.4 V *vs.* NHE) suitable for water oxidation. It has been proven by ^{18}O-labelling experiments that reactions in which Ce^{4+} act as an oxidant and manganese oxides as catalysts are "real" water-oxidation processes as bulk water provides both oxygen atoms of the produced O_2.[13,31] Our experiments were conducted in 2 ml deoxygenated aqueous solutions containing the Ca–Mn oxide and cerium ammonium nitrate. A Clark-type electrode was used for the detection of dissolved oxygen produced in these solutions. Fig. 3 shows the dissolved oxygen content in the solutions at room temperature. All compounds are active for water-oxidation while $CaMn_2O_x$-0.8-400 is by far the most active one showing a rate of 3 mmol O_2 mol Mn^{-1} s^{-1}. Furthermore, long-term oxygen evolution and stability test with gas chromatography showed that $CaMn_2O_x$-0.8-400 is active for extended time periods under harsh conditions (60 h, pH ~ 1) and can produce oxygen in second and third run at almost the

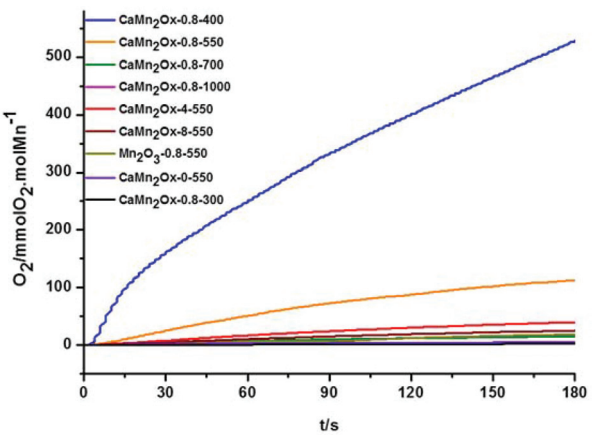

Fig. 3 Oxygen evolution in 0.5 M aqueous Ce^{4+} solution.

same rate (Fig. S14, S15 and Table S4†). The long term measurements showed lower initial oxygen evolution rates compared to the ones measured by the Clark electrode (Table 1, S4†) which might be due to the different experimental conditions and setups. The oxygen evolution rate seems also to decrease with time, which however can be explained by the consumption of the oxidant (Ce(IV)). Indeed addition of a fresh oxidant after 60 h showed that the catalyst remains active, even after long time periods. The same result is seen when a lower amount of catalyst was used (Fig. S14b and c†). Still it should be mentioned that also in this experiment a decrease in the oxygen evolution rate is found, so that also some deactivation of the catalysts over time has to be assumed.

Partially crystalline $CaMn_2O_x$-0.8-550, which is the second best catalyst, showed clearly a lower rate of 0.62 mmol O_2 mol Mn^{-1} s^{-1}. The crystalline $CaMn_2O_x$-0.8-700 is nearly inactive (oxygen evolution rate of 0.082 mmol O_2 mol Mn^{-1} s^{-1}). Two samples were prepared as references, $CaMn_2O_x$-0-550 without the use of cyanamide and Mn_2O_3-0.8-550 without calcium, in order to study the role of these two components in the catalytic activity of resulting oxides. The catalytic activity of Mn_2O_3-0.8-550 and $CaMn_2O_x$-0-550 is 6 and 21 times lower, respectively, compared to $CaMn_2O_x$-0.8-550. In both cases the resulting oxides had completely different atomic structures. In the absence of Ca^{2+}, Mn_2O_3 is formed, while in the absence of cyanamide a mixture of several crystalline phases is obtained (Fig. S5†).

In recent studies it has been suggested that layered Mn oxide phases have the highest activity in catalytic water oxidation.[20,22,30,32,33] Moreover, it has been shown that the Ca^{2+} ion is an important cofactor in biological oxygen evolution,[34] it may control charge balance and oxidation potential of the Mn_4Ca complex.[35] The Ca^{2+} ion also may act as a Lewis acid to activate water molecules for nucleophilic attack on the electrophilic oxygen atom of Mn–oxyl intermediate.[36,37] Likewise, in the layered oxides incorporation of the Ca^{2+} ion seems to be crucial to increase their activity for water oxidation.[19,20,30,38] In our case, indeed Mn_2O_3-0.8-550 showed a much lower catalytic activity than $CaMn_2O_x$-0.8-550.

The manganese oxidation state in the synthesized oxides may be among the crucial determinants of catalytic activity. The average oxidation states were estimated by means of XANES (X-ray absorption near-edge structure) analysis and are presented in Tables 1 and 2. In the oxide with the highest water-oxidation activity ($CaMn_2O_x$-0.8-400), manganese shows an average oxidation state of +3.6. It was shown for oxides used as catalysts[39] or electrocatalysts[6,17] that the performances of materials containing Mn^{3+} was superior compared to the ones with pure Mn^{4+}, which suggests that the presence of Mn^{3+} is essential for having an active catalyst. On the other hand, oxides containing Mn^{3+} only (*e.g.* Mn_2O_3-0.8-550 in our study) are also poor catalysts,[11,12] supporting that the presence of both Mn^{3+} and Mn^{4+} in a suitable ratio enhances the catalytic activity.[30]

We note that interpretation of the average oxidation state detected for the various oxides of the present investigation cannot be approached in a fully unambiguous way. An average oxidation state of +3.6 might not result from a mixed-valent $Mn^{3+/4+}$ oxide but from a mixture of a Mn^{3+} oxide, *e.g.* Mn_2O_3 or $CaMn_2O_4$, and a Mn^{4+} oxide, *e.g.* β-Mn_2O or $Ca_2Mn_3O_8$. Indeed, a mixture of microcrystalline phases of various oxides may be present in the inactive, cyanamide-free $CaMn_2O$-0-550 (see XRD data in Fig. S5a†). Yet in the oxides of high water oxidation activity ($CaMn_2O_x$-0.8-400/550), the XRD and EXAFS data are best explained in terms of a single phase of a mixed-valent $Mn^{3+/4+}$ oxide.

Manganese oxidation states

The X-ray absorption near-edge spectra (XANES) recorded at the Mn K-edge, allowed us to estimate the mean oxidation state of manganese in the samples annealed at different temperatures (Table 1 and Fig. S16†). As is evident from the energy shift of the position of the main absorption edge,[40] above 300 °C the mean formal oxidation state of Mn increases from 2 to above 3.5, indicating that most of the initial Mn^{2+} is oxidized to Mn^{4+} although some low-valence Mn ions are still present. At 1000 °C however, Mn^{4+} is reduced to Mn^{3+}, the typical Mn oxidation state found in marokite ($CaMn_2O_4$).[41] Similar Mn-oxidation state changes in mixed CaMn oxides upon annealing were observed before.[30] To follow the associated structural changes in the CaMn oxides and to identify the basic structural motifs in the amorphous catalytically active materials, we used extended range dual-edge EXAFS spectroscopy, recording spectra at both Mn and Ca K-edges (Fig. 4 and Fig. S17†).

Information on atomic structure from EXAFS

X-ray absorption spectra[40,42] were collected at the K-edges of both manganese (~6550 eV) and calcium (~4040 eV). The X-ray absorption near-edge structure (XANES; Fig. S16†) of the Mn K-edge facilitated the above estimates of the mean manganese oxidation states. The Ca-XANES (Fig. S16†) indicates significant changes in the calcium ligand environment but cannot be easily interpreted in terms of specific structural changes.

Within about 1000 eV above the respective X-ray edge, the extended X-ray absorption fine-structure (EXAFS) was detected. The EXAFS carries information on distances between the X-ray absorbing atom (Mn or Ca) and atoms of the first, second, and higher coordination spheres. The latter atoms are denoted as backscatters as they facilitate backscattering of the photoelectron wave created at the absorber atom. In the Fourier-transformed EXAFS spectra (Fig. 4), each peak corresponds to an absorber–backscatter distance, which is 0.3–0.4 Å longer than the indicated reduced distance.[40,42]

The first peak of the Fourier-transformed Mn-EXAFS at reduced distances around 1.5 Å is assignable to the oxygen atoms in the first manganese coordination sphere at distances of 1.9 Å or larger. *The second peak* at a reduced distance of 2.4 Å corresponds to a Mn–Mn distance of 2.87 Å (as revealed by EXAFS simulations) and is assignable to a pair of di-μ-oxo bridged Mn ions (edge-sharing MnO_6 octahedra). *The third peak* of Mn-only oxides (*e.g.* Mn_2O_3-0.8-550) mostly is assignable

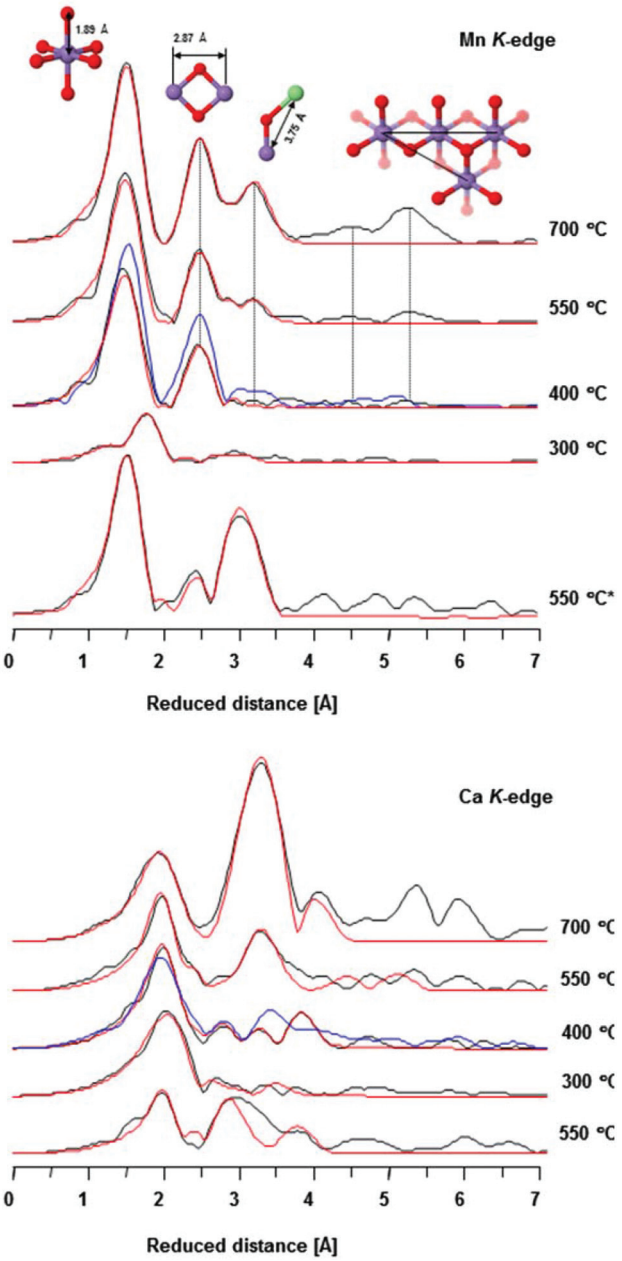

Fig. 4 Fourier-transformed EXAFS spectra measured at the Mn K-edge (top panel) and at the Ca K-edge (bottom panel). We note that the indicated 'reduced distances' are by 0.3–0.4 Å shorter than the atom–atom distances as obtained by EXAFS simulations at high precision. Black lines, experiment; red lines, simulations; blue line, spectra of the catalytically active $CaMn^{IV}_{1.6}Mn^{III}_{0.4}O_{4.5}(OH)_{0.5}$ oxide investigated in ref. 29. The asterisk (550 °C*) indicates the sample prepared without cyanamide. The structural motifs corresponding to each of the main peaks are schematically depicted (Mn in magenta, Ca in green, O in red).

to pairs of mono-μ-oxo bridged Mn ions with typical distances close to 3.4 Å. In the MnCa oxides however, there are contributions to the third EXAFS peak resulting from calcium ions connected by several bridging oxygens to manganese ions. *The two long-distance peaks* at a reduced distance of about 5.3 and 4.6 Å are assignable to backscattering by manganese ions in the fourth and fifth coordination spheres of the X-ray absorbing manganese (see structural motif indicated in Fig. 4); the presence of these two peaks is indicative of long-range order (crystallinity or low level of amorphicity).

Visual inspection of the Mn-EXAFS spectra before (Fig. S17†) or after Fourier-transformation (Fig. 4) reveals that for increasing the temperature from 400 *via* 550 to 700 °C, the long-range order increases (increased long-distance peaks, Fig. 4; increased EXAFS amplitudes at higher *k*-values, Fig. S17†). However, the basic shape of the spectra remains the same suggesting that the increase in calcination temperature from 400 to 700 °C causes lowered amorphicity (higher crystallinity) without changing the central structural motifs present in the first and second coordination spheres of the Mn ions. For calcination temperatures below 400 °C, no metal–metal distances are resolved suggesting that the metal ions are not interconnected by bridging oxides but merely coordinated to water molecules and cyanamide-derived ligands.

In clear contrast, the Ca-EXAFS differs pronouncedly between oxides calcined at 400 °C and 700 °C (Fig. 4 and Fig. S17†), indicating a pronounced change in the ligand environment of the X-ray absorbing calcium ions. This can be explained as follows. Most likely the calcium ions are located in the space between layers of edge-sharing MnO_6 octahedra. In the highly ordered and largely dehydrated oxide created by calcination at 700 °C and resembling crystalline $Ca_2Mn_3O_8$ closely, the majority of calcium ions may directly interconnect layers of edge-sharing MnO_6 octahedra (see Fig. S12,† left panel). However in the water-rich oxide obtained by moderate calcination at 400 °C, the calcium ions are coordinated to several water molecules of the interlayer space.

Precise atom–atom distances were obtained by simulating simultaneously the Mn-EXAFS and the Ca-EXAFS using a joint-fit approach described before.[30] The simulated spectra are shown in Fig. S17† and Fig. 4; simulation parameters are given in Table S5 and Fig. S18.† For the $CaMn_2O_x$-0.8-700 oxide, the EXAFS simulation results confirm the prevalence of the $Ca_2Mn_3O_8$ structure indicated by the XRD, even though the Ca : Mn stoichiometries differ. The distances between μ-oxo bridged Mn–Mn and Mn–Ca pairs as determined by the EXAFS simulations agree well with the corresponding distances of the crystallographic model.[28,29] Two Mn–Ca distances of 3.3 Å and 3.7 Å are resolved by EXAFS simulations. They are assignable to $CaMn_3(\mu\text{-}O)_4$ structures resembling distorted cubanes (3.3 Å) and to a motif of Ca ions capping missing layer-building Mn ions (3.7 Å, see Fig. 5). The characteristic 2.88 Å distance for di-μ-oxo connected Mn ions of layered oxides[43] is well resolved, as well as Ca–Ca distances of $Ca_2Mn_3O_8$.

Both XRD and XAS strongly suggest the presence of $Ca_2Mn_3O_8$ in $CaMn_2O_x$-0.8-700. There are two possible explanations for the mismatch in the Ca : Mn stoichiometry (1 : 2 in the synthesized oxide *versus* 2 : 3 in $Ca_2Mn_3O_8$): (a) aside from $Ca_2Mn_3O_8$ crystallites, a largely amorphous CaMn oxide with a low Ca content is present in $CaMn_2O_x$-0.8-700. (b) The $Ca_2Mn_3O_8$ structure may be viewed as layers of edge-sharing MnO_6 octahedra with Mn-vacancies capped by calcium ions;

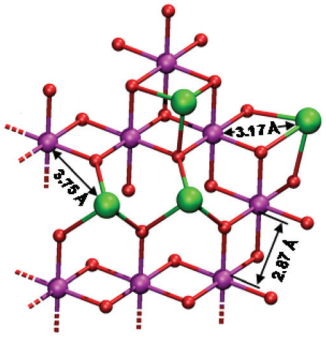

Fig. 5 Structural model of a fragment from catalytically active CaMn oxide. The presence of distances close to 3.8 and 3.2 Å is suggested by the EXAFS data collected at the Ca K-edge, but is not resolved (3.8 Å) or not well resolved (3.2 Å) in the Mn-EXAFS simulations (see Table S5†). The first coordination sphere of calcium is complemented either by μ-oxo bridges to manganese ions or by water molecules. The color code is the same as in Fig. 4.

the removal of capping calcium ions and filling of the corresponding Mn-vacancies could result in a major change in the Ca : Mn stoichiometry, without modification of other unit cell parameters.

The latter explanation (that is, (b)) is in good agreement with the EXAFS results, but also (a) cannot be ruled out definitively. The EDS mapping supports (b) because two distinct phases differing in the Ca : Mn stoichiometry are not detectable. However, the spatial resolution of the presented EDS-mapping data might be insufficient to resolve different phases in neighbouring small crystallites. Whether (b) is in conflict with the XRD powder diffraction data remains an open question. Conclusive XRD analysis of amorphous materials or crystallites with an imperfect crystalline order requires extensive simulations which are beyond the scope of the present study.

Distances similar to the ones found in $CaMn_2O_x$-0.8-700 are also found in $CaMn_2O_x$-0.8-550 (Table S5†). However the coordination numbers for the metal–metal distances are lower suggesting prevalence of a clearly less ordered structure, that is, a clearly higher level of amorphicity in $CaMn_2O_x$-0.8-550.

At 400 °C calcination, the coordination numbers of the 2.9 Å Mn–Mn distance are even lower (lower amplitude of second Fourier peak). All Mn–Mn distances exceeding 3 Å result in small contributions to the EXAFS only (see Fig. 4) indicating an especially high level of amorphicity. Consequently the Mn-EXAFS simulation results of Table S5† which relate to Mn–Mn/Ca distances exceeding 3 Å are of low significance. It is likely that the Mn–Ca motifs with characteristic Mn–Ca distances of 3.2 Å (cubane) and 3.7 Å (Ca capping Mn-layer-vacancy) are also present in $CaMn_2O_x$-0.8-400, but clearly less frequently than in the oxides calcined at 550 and 700 °C. It is noteworthy that the amorphicity of $CaMn_2O_x$-0.8-400 is even higher than observed for oxides previously synthesized in the absence of cyanamide (blue lines in Fig. 4).[19]

In summary, calcination at temperatures higher than 300 °C induces the formation of high-valent $Mn^{III/IV}$ oxides which consist of vacancy-rich layers of edge-sharing MnO_6 octahedra. These oxides may be considered as being relatives of layered oxides with one layer (birnessite) or two layers (buserite) of water molecules and cations interconnecting MnO_2 layers.[44] For calcinations at 400 °C, the MnCa oxide is highly disordered, providing an especially high number of both protonatable (and potentially reactive) μ_2-O(H) bridges and terminal water-coordination sites.[45]

This may explain the especially high water-oxidation activity of $CaMn_2O_x$-0.8-400, which exceeds the activity of better ordered MnCa oxides previously synthesized in the absence of cyanamide.[19] At higher calcination temperatures (550 and 700 °C), the structure becomes increasingly well-ordered and approaches the 'parent structure' of crystalline $Ca_2Mn_3O_8$ closely.

Without the addition of cyanamide but using otherwise the same synthesis protocol, an entirely different structure is formed, which is dominated by mono-μ-oxo bridging between manganese ions. This structure exhibits higher crystallinity and shows similarities to the β-MnO_2 crystalline phase (1 × 1 tunnel Mn oxides),[46] but not to the layered birnessite-like oxides.[47,48]

Conclusions

We reported a simple, robust and easily reproducible synthetic protocol resulting in a highly active mixed MnCa oxide catalyst for water oxidation. CaMn oxides have been prepared by adding cyanamide to the Ca and Mn precursor salts and subsequent thermal treatment. Cyanamide or more probably one of its condensation and decomposition products acts as a porogen and foam-like porous CaMn oxides are observed. Analysis of crystal and atomic structures of the resulting CaMn oxides show that besides pore formation and surface area, cyanamide also strongly influences the prevalent Mn oxidation state, the atomic structure, and the level of amorphicity. It is generally assumed that all these factors can influence the catalytic activity of CaMn oxides for water oxidation, while the surface area seems to be no decisive factor determining the water oxidation activity in amorphous materials (Fig. S19†). In other words the presented results indicate that the catalytic reaction may take place also at the active centres formed in the bulk phase of the amorphous materials. At the atomic level, a structure containing poorly ordered layered fragments built from di-μ-oxo connected Mn ions (in mixed oxidation states of +3 and +4) and coordinatively non-saturated oxygens in bridging positions establish the catalytic properties of the synthetic oxides. Incorporation of Ca^{2+} in the structure presumable contributes to the achieved high catalytic rates.

Acknowledgements

Financial support from the Cluster of Excellence "Unifying Concepts in Catalysis" (EXL 31411) and the project "Nachhaltige Chemie (Sustainable Chemistry)" funded by the senate of

Berlin is gratefully acknowledged. We thank Dr P. Chernev, Katharina Klingan and J. Heidkamp for their essential contributions in the XAS experiments. We acknowledge support by the BESSY synchrotron (Berlin) operated by the Helmholtz-Zentrum Berlin (HZB), specifically the excellent technical support by M. Mertin and Dr F. Schäfers. The authors express their gratitude to Jörg Nissen from the Department of Electron Microscopy ZELMI, TU Berlin for the SEM measurements.

References

1 H. Dau, C. Limberg, T. Reier, M. Risch, S. Roggan and P. Strasser, *ChemCatChem*, 2010, **2**, 724–761.
2 C. Minero, E. Lorenzi, E. Pramauro and E. Pelizzetti, *Inorg. Chim. Acta*, 1984, **91**, 301–305.
3 F. A. Frame, T. K. Townsend, R. L. Chamousis, E. M. Sabio, T. Dittrich, N. D. Browning and F. E. Osterloh, *J. Am. Chem. Soc.*, 2011, **133**, 7264–7267.
4 M. W. Kanan and D. G. Nocera, *Science*, 2008, **321**, 1072–1075.
5 A. Harriman, I. J. Pickering, J. M. Thomas and P. A. Christensen, *J. Chem. Soc., Faraday Trans. 1*, 1988, **84**, 2795–2806.
6 M. Morita, C. Iwakura and H. Tamura, *Electrochim. Acta*, 1977, **22**, 325–328.
7 K. Mette, A. Bergmann, J.-P. Tessonnier, M. Hävecker, L. Yao, T. Ressler, R. Schlögl, P. Strasser and M. Behrens, *ChemCatChem*, 2012, **4**, 851–862.
8 M. Dincă, Y. Surendranath and D. G. Nocera, *Proc. Natl. Acad. Sci. U. S. A.*, 2010, **107**, 10337–10341.
9 V. Y. Shafirovich and A. E. Shilov, *Kinet. Katal.*, 1979, **20**, 1156–1162.
10 R. Brimblecombe, A. Koo, G. C. Dismukes, G. F. Swiegers and L. Spiccia, *J. Am. Chem. Soc.*, 2012, **132**, 2892–2894.
11 V. B. R. Boppana and F. Jiao, *Chem. Commun.*, 2011, **47**, 8973–8975.
12 M. M. Najafpour, F. Rahimi, M. Amini, S. Nayeri and M. Bagherzadeh, *J. Chem. Soc., Dalton Trans.*, 2012, **41**, 11026–11031.
13 A. Iyer, J. Del-Pilar, C. K. King ondu, E. Kissel, H. F. Garces, H. Huang, A. M. El-Sawy, P. K. Dutta and S. L. Suib, *J. Phys. Chem. C*, 2012, **116**, 6474–6483.
14 F. Cheng, J. Shen, B. Peng, Y. Pan, Z. Tao and J. Chen, *Nat. Chem.*, 2011, **3**, 79–84.
15 Y. Gorlin and T. F. Jaramillo, *J. Am. Chem. Soc.*, 2010, **132**, 13612–13614.
16 N. P. Luneva, V. Y. Shafirovich and A. E. Shilov, *J. Mol. Catal. A: Chem.*, 1989, **52**, 49–62.
17 S. Trasatti, *J. Electroanal. Chem. Interfacial Electrochem.*, 1980, **111**, 125–131.
18 H. Dau, I. Zaharieva and M. Haumann, *Curr. Opin. Chem. Biol.*, 2012, **16**, 3–10.
19 M. M. Najafpour, T. Ehrenberg, M. Wiechen and P. Kurz, *Angew. Chem., Int. Ed.*, 2010, **49**, 2233–2237.
20 M. Wiechen, I. Zaharieva, H. Dau and P. Kurz, *Chem. Sci.*, 2012, **3**, 2330–2339.
21 K. Kailasam, J. D. Epping, A. Thomas, S. Losse and H. Junge, *Energy Environ. Sci.*, 2011, **4**, 4668–4674.
22 I. Zaharieva, P. Chernev, M. Risch, K. Klingan, M. Kohlhoff, A. Fischer and H. Dau, *Energy Environ. Sci.*, 2012, **5**, 7081–7089.
23 M. Schwarze, D. Stellmach, M. Schröder, K. Kailasam, R. Reske, A. Thomas and R. Schomäcker, *Phys. Chem. Chem. Phys.*, 2013, **15**, 3466–3472.
24 A. Thomas, A. Fischer, F. Goettmann, M. Antonietti, J. O. Muller, R. Schlogl and J. M. Carlsson, *J. Mater. Chem.*, 2008, **18**, 4893–4908.
25 B. V. Lotsch and W. Schnick, *Chem.–Eur. J.*, 2007, **13**, 4956–4968.
26 N. N. Greenwood and A. Earnshaw, *Chemistry of the Elements*, Butterworth-Heinemann, Oxford, 1997.
27 C. M. Julien, M. Massot and C. Poinsignon, *Spectrochim. Acta, Part A*, 2004, **60**, 689–700.
28 G. B. Ansell, M. A. Modrick, J. M. Longo, K. R. Poeppeimeler and H. S. Horowitz, *Acta Crystallogr., Sect. B: Struct. Crystallogr. Cryst. Chem.*, 1982, **38**, 1795–1797.
29 T. R. White, W. S. Glaunsinger, H. S. Horowitz and J. M. Longo, *J. Solid State Chem.*, 1979, **29**, 205–214.
30 I. Zaharieva, M. M. Najafpour, M. Wiechen, M. Haumann, P. Kurz and H. Dau, *Energy Environ. Sci.*, 2011, **4**, 2400–2408.
31 D. Shevela, S. Koroidov, M. M. Najafpour, J. Messinger and P. Kurz, *Chem.–Eur. J.*, 2011, **17**, 5415–5423.
32 R. K. Hocking, R. Brimblecombe, L.-Y. Chang, A. Singh, M. H. Cheah, C. Glover, W. H. Casey and L. Spiccia, *Nat. Chem.*, 2011, **3**, 461–466.
33 B. A. Pinaud, Z. Chen, D. N. Abram and T. F. Jaramillo, *J. Phys. Chem. C*, 2011, **115**, 11830–11838.
34 H. Dau and M. Haumann, *Coord. Chem. Rev.*, 2008, **252**, 273–295.
35 E. Y. Tsui, R. Tran, J. Yano and T. Agapie, *Nat. Chem.*, 2013, **5**, 293–299.
36 J. Limburg, V. A. Szalai and G. W. Brudvig, *J. Chem. Soc., Dalton Trans.*, 1999, 1353–1362.
37 M. J. B. V. L. Pecoraro, M. T. Caudle, W.-Y. Hsieh and N. A. Law, *Pure Appl. Chem.*, 1998, **70**, 925–929.
38 M. M. Najafpour, *J. Chem. Soc., Dalton Trans.*, 2011, **40**, 3793–3795.
39 F. Jiao and H. Frei, *Chem. Commun.*, 2010, **46**, 2920–2922.
40 H. Dau, P. Liebisch and M. Haumann, *Anal. Bioanal. Chem.*, 2003, **376**, 562–583.
41 S. Zouari, L. Ranno, A. Cheikh-Rouhou, O. Isnard, M. Pernet, P. Wolfers and P. Strobel, *J. Alloys Compd.*, 2003, **353**, 5–11.
42 J. E. Penner-Hahn, *Coord. Chem. Rev.*, 1999, **190–192**, 1101–1123.
43 M. Villalobos, B. Lanson, A. Manceau, B. Toner and G. Sposito, *Am. Mineral.*, 2006, **91**, 489–502.

44 J. E. Post, *Proc. Natl. Acad. Sci. U. S. A.*, 1999, **96**, 3447–3454.
45 H. Dau, C. Limberg, T. Reier, M. Risch, S. Roggan and P. Strasser, *ChemCatChem*, 2010, **2**, 724–761.
46 R. W. G. Wyckoff, *Crystal Structures*, Interscience Publishers, New York, 1963.
47 B. M. Tebo, J. R. Bargar, B. G. Clement, G. J. Dick, K. J. Murray, D. Parker, R. Verity and S. M. Webb, *Annu. Rev. Earth Planet. Sci.*, 2004, **32**, 287–328.
48 T. G. Spiro, J. R. Bargar, G. Sposito and B. M. Tebo, *Acc. Chem. Res.*, 2010, **43**, 2–9.